Drag and lift forces on microscopic bubbles entrained by a vortex

G. Sridhar and J. Katz
Department of Mechanical Engineering, The Johns Hopkins University, Baltimore, Maryland 21218

(Received 30 November 1993; accepted 20 September 1994)

The forces that act on bubbles as they are entrained by a vortex are measured using particle image velocimetry. Triple exposure images are used to measure the velocity and acceleration of the fluid and the bubbles simultaneously. Distinction between phases is achieved by using fluorescent particles as liquid flow tracers. The buoyancy, pressure, and inertia forces are computed from the data, while the drag and the lift forces are determined from a force balance on each bubble. It is found that in the present range of bubble diameters, 500 μm$<d<$800 μm, and Reynolds numbers, 20$<$Re$<$80, the drag on a bubble is similar to that on a solid body. Vorticity does not have a significant effect on the drag coefficient. The lift coefficients are significantly higher than currently available analytical and numerical estimates. The coefficients are independent of the Reynolds number and are proportional to the fourth root of the local vorticity. Estimates of the Bassett force show that it can be neglected in the present experiment. Computed bubble trajectories, based on the measured lift and drag coefficients, compare well with experimental observations. © *1995 American Institute of Physics.*

I. INTRODUCTION

Very little information is currently available on the forces that act on bubbles as they are entrained by vortices. Most of the past studies have focused on measuring the drag force on bubbles rising in quiescent liquids (Clift *et al.*[1]). They show that the drag coefficient of small bubbles in common untreated water, typically equals that of solid spheres (Harper[2]), due to the presence of trace impurities that "solidify" the gas–water interface. The lift force on bubbles has been studied analytically by Auton *et al.*,[3] assuming a potential flow model. They conclude that the lift is proportional to the relative velocity and the local vorticity. The only known direct measurements of the lift on bubbles are reported by Naciri,[4] who computed the forces from the equilibrium positions of bubbles within a rotating cylinder containing water. His data, which is measured at a single dimensionless vorticity, differs significantly from Auton's results.

Since information on the forces on bubbles is limited, it is helpful to review the data available on solid spheres. The forces on a smooth, solid sphere, moving at a constant velocity in an otherwise undisturbed fluid, have been investigated extensively. It is established that the drag force is well represented by the standard drag coefficient curve (Clift *et al.*[1]) and that the added mass coefficient is 0.5 for Stokes and potential flows. An exact mathematical expression for the Bassett or History force is also known at low Reynolds numbers (Bassett;[5] Maxey and Riley[6]). The effect of acceleration and Reynolds numbers on drag, added mass, and Bassett forces have also been investigated, though the results are at times contradictory. Temkin and Mehta[7] report that the unsteady drag coefficient on a decelerating sphere is higher than the corresponding steady-state value at the same Reynolds number and vice versa. However, recent numerical simulations by Li and Boulos[8] and experiments by Odar and Hamilton[9] and Tsuji *et al.*[10] suggest that the drag coefficient equals the steady-state value even in unsteady flows. The difference occurs because C_d, the drag coefficient, as defined by Temkin and Mehta,[7] represents the combined effects of viscous drag, acceleration reaction, and "history" effects. Experiments by Odar and Hamilton[9] and Odar[11,12] also indicate that while the drag coefficient is not affected by acceleration (but depends on the Reynolds number), the added mass coefficient decreases and the Bassett coefficient increases with acceleration. Both coefficients are independent of the Reynolds number and converge to their Stokes flow estimates in the limit of zero acceleration. However, in contradiction to these conclusions, the results of Chang[13] indicate that the added mass coefficient is independent of both the Reynolds number and the acceleration number. The Bassett force (Mei *et al.*;[14] Mei and Adrian[15]), on the other hand, is not independent of the Reynolds number, but decreases as the Reynolds numbers increases above unity. Thus, there still is not a clear, definite theory that describes the forces on spheres in unsteady flows.

An analytical solution for the lift force on a free solid sphere in an unbounded, linear shear flow is provided by Saffman.[16] When $\mathrm{Re}_S \ll \mathrm{Re}_G^{0.5} < 1$, where $\mathrm{Re}_S = U_{\mathrm{rel}} d/\nu$ and $\mathrm{Re}_G = G d^2/\nu$ (U_{rel} is the particle slip velocity, d is the particle diameter, G is the velocity gradient, and ν is the kinematic viscosity), the lift force is proportional to the relative velocity and to the square root of the shear rate. McLaughlin[17] extends the Saffman analysis to situations where Re_S is not small compared to Re_G and shows that the magnitude of this force decreases to small values as Re_S increases (but still below 1.0). Harper and Chang[18] and Drew[19] generalized Saffman's analysis to arbitrary bodies in a linear shear flow and for the case of a small sphere in a two-dimensional (2-D) strain flow. Cox and Brenner[20] considered the lift force on a particle in a wall bounded flow. They assumed that $\mathrm{Re}_l \ll 1$, where Re_l is the Reynolds number based on the distance "l" of the particle from the wall, and derived a general expression for the lift force in terms of a Green's function. The transverse force on a spinning sphere moving in a stationary viscous fluid has been obtained analytically by Rubinov and Keller[21] for Reynolds numbers less than 1.0. In this case, the force is proportional to the rotation rate and the mean velocity of the sphere. At "intermediate Reynolds numbers" ($0<\mathrm{Re}<100$), the only available data are the computations by Dandy and Dwyer[22] of the flow around a *fixed* sphere located in shear flow. The results indicate that the lift force is proportional to the local shear rate and the square of the velocity. The lift coefficient decreases rapidly to very low values (less than 0.03) for Reynolds number greater than 20. These results are smaller than Naciri's[3] measurements with bubbles (as well as the results presented in the present paper) by an order of magnitude. At Reynolds numbers exceeding 500, the only available data come from experiments involving measurements of the trajectories of spinning spheres in quiescent fluids (Barkla and Auchterlonie;[23] Tri *et al.*;[24] Tsuji *et al.*[10]). Their lift coefficients are comparable in magnitude to Naciri's[4] results, but trends with vorticity vary, as will be discussed later in this paper.

The present study is part of our ongoing effort to predict the entrainment of bubbles by vortex structures (vortex rings in the present study). Such a task requires knowledge of the drag, lift, pressure, inertia, and Bassett forces that act on a bubble over a range of Reynolds numbers. Since the available literature provides a limited database, in Sec. II of this paper we directly measure the drag and lift forces on a bubble and compute the corresponding coefficients. The procedure involves measurement of the pressure, inertia, and buoyancy forces on each bubble, and balancing their resultant with the lift and drag forces. The pressure and inertia are calculated from the velocity and acceleration of the bubble and the fluid surrounding it. Both are measured using particle image velocimetry (PIV). Buoyancy is computed from the bubble size. At this stage, the experiments are limited to Reynolds numbers (based on the relative velocity) below 100, and bubble diameters below 1 mm. The results show that the drag force on bubbles in nonuniform flow fields (at least when the flow scales are larger than the bubble diameter) follows the same trends as bubbles in quiescent liquids. The magnitude of the lift coefficients and their trends with vorticity are found to be considerably different from the available analytical and numerical predictions. They do agree, however, with Naciri's[4] measurements. The Bassett force is also estimated and is found to be negligible in most cases. In Sec. III of this paper the measured coefficients are used to predict the trajectory of a bubble. The results compare well with experimental observations.

Details of the techniques and procedures used to obtain the drag and lift forces, as well as the numerical scheme for predicting the bubble trajectory, are provided in the following sections.

II. MEASUREMENT OF DRAG AND LIFT FORCES

A. Experimental setup

The experimental apparatus (Fig. 1) consists of a vortex ring generator, a bubble injector, instrumentation associated with PIV, and a control system to regulate the experiment. Each subsystem is described below.

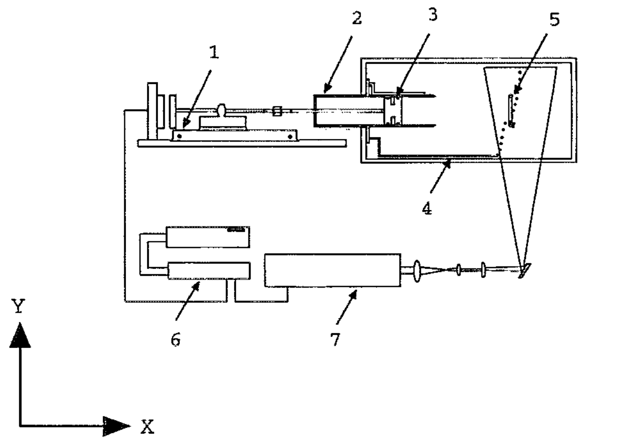

FIG. 1. Schematic of the experimental facility.

1. Vortex ring generator

Horizontally traveling vortex rings are generated by moving a piston within a cylinder immersed in water (Fig. 1). The dimensions of the water tank are 2 m$\times$0.8 m$\times$0.5 m. The piston diameter and stroke length are both 0.1 m. The piston is driven by a pneumatic actuator capable of moving at a maximum speed of 2 m/s. The air pressure to the actuator (up to 690 kPa) is regulated by two solenoid valves, and an electromagnet is used for restraining the piston prior to each experiment. For reference purposes, when the piston speed is 15 cm/s (as was used in some of the experiments), the ring is typically 12 cm in diameter, its strength is 95 $\mathrm{cm^2/s}$ and it is convected downstream at 6 cm/s. The lip of the cylinder is fitted with three orifices for injecting tracer particles into its cavity.

2. Bubble generator and size distribution

A train of uniform bubbles are introduced in the path of the vortex rings, at its center plane, 0.5 m from the tip of the cylinder. The bubbles are generated by forcing air through 5–50 μm injectors created by stretching glass tubes under heat (Ran and Katz[25]). The bubble size and injection rate are controlled by varying the injector diameter and the air pressure.

The diameter of the bubbles are measured by recording holograms of the bubble train using an inline ruby laser holocamera (refer to Ran and Katz[25] for details of the holocamera). The holograms are reconstructed and scanned with a CCD camera at magnifications up to 200$\times$, from which the sizes are measured manually. When the flow field is not flooded with particles, it is possible to measure the bubble diameter at an uncertainty level, varying between 2 and 5 μm. In the range of Reynolds numbers (20–80) and Eötvös number (0.086) covered in the present study, the bubbles should remain almost spherical ($\pm$5%, Clift *et al.*[1]), as was

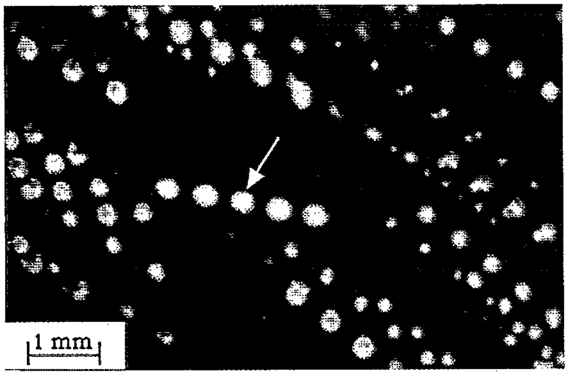

FIG. 2. Typical five exposure image of bubble and particle traces. The bubble is indicated by the arrow. (In the original photograph they have different colors.)

also confirmed by the holograms. Thus, it is possible to measure the mean diameter of the bubble with a relative uncertainty of 1%.

3. PIV system and procedures

Particle image velocimetry (PIV) is utilized to measure the velocities and accelerations of the fluid and bubbles simultaneously. As described in Sridhar *et al.*,[26] the flow field is seeded with microscopic (20 μm–30 μm), neutrally buoyant (specific gravity 0.95–1.05), fluorescent particles, and the central plane of the vortex ring is illuminated with a 1 mm thick Cu-vapor laser sheet. The dye in the particles fluoresces at 573 nm, namely in the yellow range, while the bubbles scatter the incident light (512 nm) and appear green. This difference in colors enables us to distinguish the two phases. The laser is pulsed at 300 Hz (the pulse width is 30 ns), and images are recorded with a 35 mm camera, that has a maximum frame rate of 65 Hz. The laser pulses and camera speed are adjusted so that each frame is exposed at least three times. The recorded film is digitized with a Nikon LS3500 film scanner and the velocities and accelerations are measured using a correlation technique outlined below.

The triple exposure images are digitized at a magnification of 1300 pixels/cm. A sample image of particle and bubble traces is presented in Fig. 2 (the original is in color). At this magnification the diameters of the particle and bubble traces are typically 30 and 40 pixels, respectively. Note that the ratio between these sizes is not an indicator of the diameter ratio, which is at least 20:1. The particles appear larger because they fluoresce at a relatively high intensity while the bubble traces appear smaller since the light reflected from them is observed normal to the direction of illumination. For reasons that will be discussed shortly, four particles around the bubble are selected and the rest are removed from the image [Figs. 3(a)–7(a)]. The distance between successive traces is determined by selecting small sections of the image, that include these traces, and cross-correlating between them. The correlation function is defined as

$$F(m,n)=\sum_i \sum_j I(i,j)I(i+m,j+n), \tag{1}$$

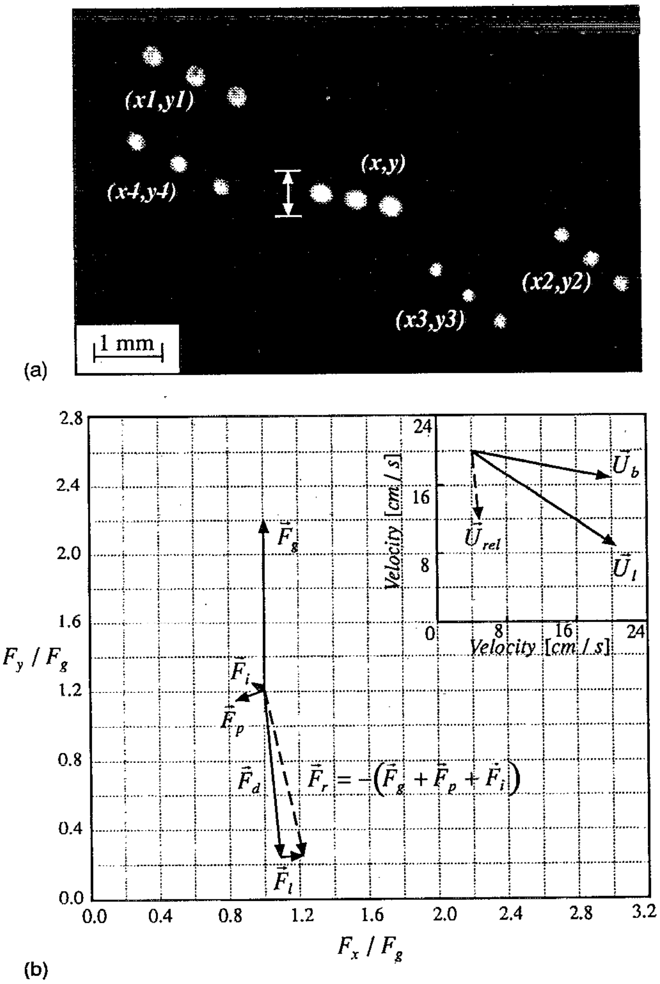

FIG. 3. (a) Triple trace image of a bubble and four particles selected from Fig. 2. The actual bubble diameter, 710 μm, is indicated with the white arrow. (b) Corresponding force and velocity diagrams of the bubble. $\mathbf{F}_g$, $\mathbf{F}_p$, $\mathbf{F}_i$, $\mathbf{F}_d$, and $\mathbf{F}_l$ are the buoyancy, pressure gradient, inertia, drag, and lift forces, respectively.

where $I(i,j)$ is the intensity of the pixel located at (i,j). The displacement is determined from the location of the correlation peak. Subpixel accuracy is obtained by fitting a 2-D Gaussian surface between the discrete values of $F(m,n)$, and determining the maximum of the interpolated function. Use of different interpolation methods, such as polynomials of various powers, do not have a significant impact on the results. Repeated examinations of the same data, while varying the image enhancement and interpolation methods lead to the conclusion that, at the present magnification, the uncertainty in determining the particle displacement is 0.4 pixels. This value is quite conservative and represents the maximum deviation between results.

4. Calculation of fluid velocity, acceleration, and vorticity

The fluid velocity at the location of the bubble, $\mathbf{U}_l$, is calculated from the velocity of the four particles selected around it. It is important to ensure that the particle motion is affected very little by the flow induced by the bubble slip and represents the undisturbed local flow. Thus, we select par-

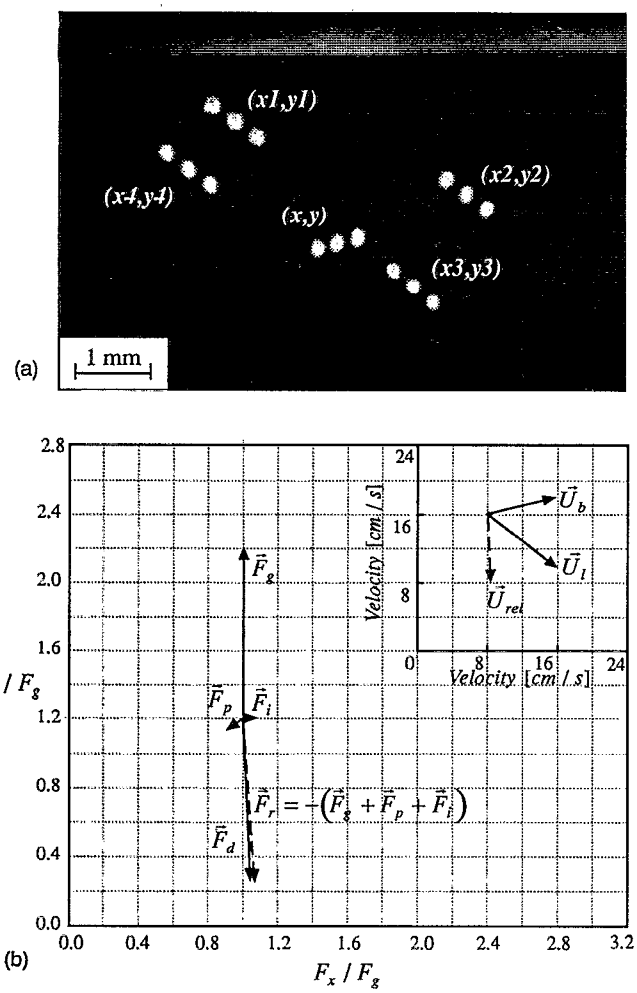

FIG. 4. (a) Image of a 710 μm diameter bubble and traces of 20 μm particles in a low vorticity region. (b) Corresponding force balance. Notations are the same as in Fig. 3.

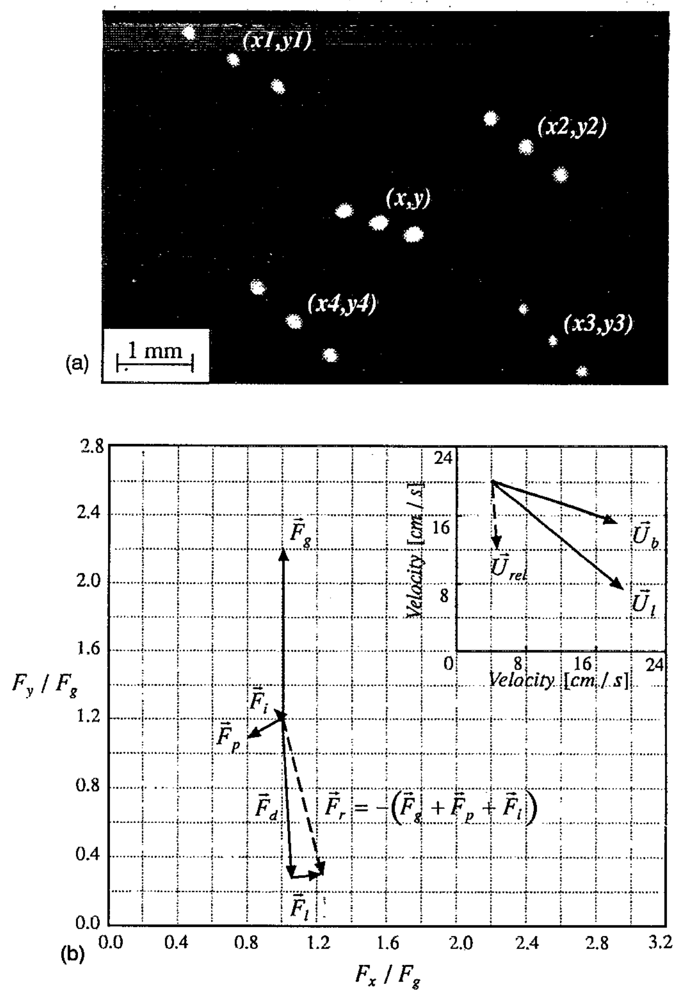

FIG. 5. (a) Image of a 710 μm diameter bubble and traces of 20 μm particles located where $|\mathbf{F}_p|/|\mathbf{F}_g|=0.23$. (b) Force balance on the bubble.

ticles whose distances from the bubble are 2–4 bubble diameters. At this distance, using a potential flow model, the local velocity varies by at most 2% due to the presence of the bubble. In most cases, depending on the orientation, the effect is lower than our error limit. To estimate $\mathbf{U}_l$, the particle locations $[(x_1,y_1),(x_2,y_2),(x_3,y_3),(x_4,y_4)]$, are mapped onto a unit square ($0<\eta,\ \zeta<1$) using the transformation:

$$x=x_1(1-\eta)(1-\zeta)+x_2(1-\zeta)\eta+x_3\eta\zeta+x_4\zeta(1-\eta),$$
$$y=y_1(1-\eta)(1-\zeta)+y_2(1-\zeta)\eta+y_3\eta\zeta+y_4\zeta(1-\eta). \tag{2}$$

After determining the location of the bubble in this plane, the fluid velocity is estimated using linear interpolation:

$$\mathbf{U}_l=\mathbf{U}_{l,1}(1-\eta)(1-\zeta)+\mathbf{U}_{l,2}(1-\zeta)\eta+\mathbf{U}_{l,3}\eta\zeta+\mathbf{U}_{l,4}\zeta(1-\eta). \tag{3}$$

Since each particle is exposed three times, the local fluid acceleration is determined by comparing the displacement vectors at two successive instants of time. The particle accelerations are also interpolated [Eqs. (2) and (4)] to determine the fluid acceleration at the location of the bubble,

$$\mathbf{a}_l=\mathbf{a}_{l,1}(1-\eta)(1-\zeta)+\mathbf{a}_{l,2}(1-\zeta)\eta+\mathbf{a}_{l,3}\eta\zeta+\mathbf{a}_{l,4}\zeta(1-\eta). \tag{4}$$

The vorticity in the vicinity of the bubble is estimated by computing the circulation around a contour defined by the four particles. Assuming the local vorticity (ω) to be constant within this region, it is given by

$$\omega=\frac{1}{2\Delta A}\left((\mathbf{U}_{l,1}+\mathbf{U}_{l,4})\cdot(\mathbf{x}_{l,1}-\mathbf{x}_{l,4})+\sum_{1}^{3}(\mathbf{U}_{l,i}+\mathbf{U}_{l,i+1})\cdot(\mathbf{x}_{l,i+1}-\mathbf{x}_{l,i})\right), \tag{5}$$

where $\mathbf{U}_{l,i}$ is the velocity of a particle located at $\mathbf{x}_{l,i}$, and ΔA is the area of the enclosed contour.

As discussed in Appendix A, typical uncertainties for the bubble and interpolated fluid velocities are 0.6%–0.9% and 0.4%–2.3%, respectively. Uncertainties in acceleration vary considerably, between 9% to 48% for the bubble (high levels of uncertainty occur only in regions with low acceleration), and between 6% to 12% for the fluid. Typical relative errors

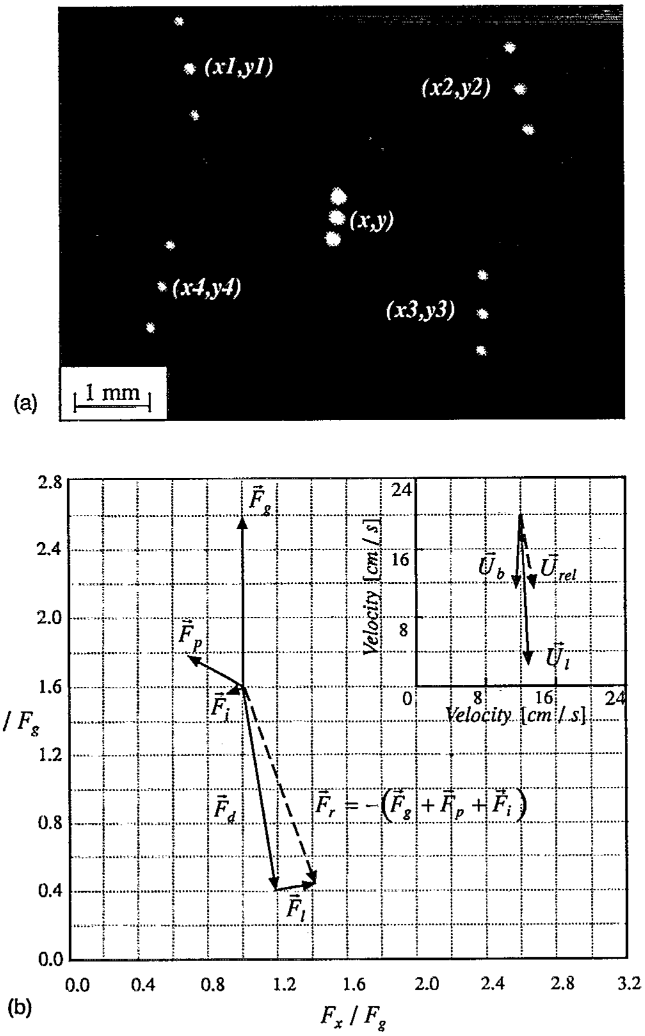

FIG. 6. (a) Image of a 710 μm diameter bubble and traces of 20 μm particles located where $|\mathbf{F}_p|/|\mathbf{F}_g|=0.35$. (b) Force balance on the bubble.

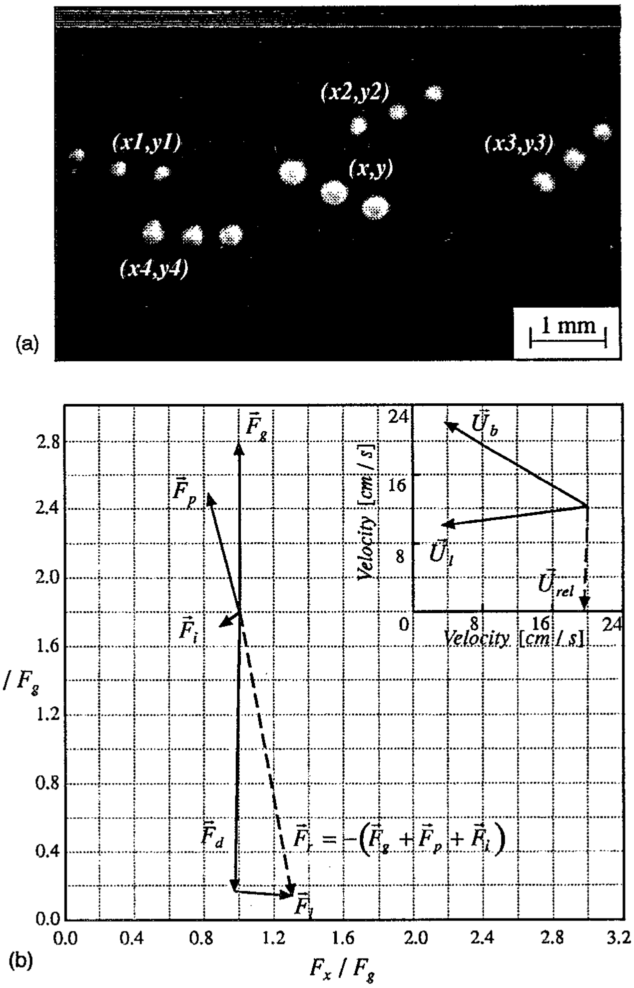

FIG. 7. (a) Image of a 710 μm diameter bubble and traces of 20 μm particles located where $|\mathbf{F}_p|/|\mathbf{F}_g|=0.73$. (b) Force balance on the bubble.

of the vorticity vary between 1.1%, close to the vortex core, and 10% in the outer perimeter of the vortex.

5. Control and sequence of events during an experiment

The entire experiment is controlled with a personal computer and external electronics, that provide the proper signals to the laser, camera, actuator, restrainer, etc. At the beginning of an experiment the piston is retracted and particles are injected into the cylinder. The solenoid valves to the actuator are opened, pushing the piston forward and generating a vortex ring. As the ring approaches the bubble train, the camera is activated and the laser is pulsed at 300 Hz. Images are recorded until the ring moves out of the light sheet, providing about 30 frames with useful data. The piston is then retracted and the experiment is repeated after allowing sufficient time for the liquid to become quiescent. Holograms of the bubble train are recorded prior to and at the end of each experiment to ensure that the bubble size has not changed.

B. Forces acting on a bubble

The equation for the balance of forces on a bubble can be written as

$$\mathbf{0}=\mathbf{F}_g+\mathbf{F}_p+\mathbf{F}_i+\mathbf{F}_b+\mathbf{F}_d+\mathbf{F}_l, \tag{6}$$

where the terms on the right-hand side are, in order, buoyancy, pressure, inertia, Bassett, drag, and lift. Outlined below are the methods used to calculate these forces and the associated errors in the measurements.

Buoyancy: With the bubble radius, a, available from the holograms, the buoyancy force is

$$\mathbf{F}_g=\tfrac{4}{3}(\rho_b-\rho_l)\mathbf{g}\pi a^3, \tag{7}$$

where ρ_l is the liquid density, ρ_b is the bubble density, and $\mathbf{g}$ is the acceleration due to gravity. Due to the uncertainty in the bubble size (<1%), the accuracy in the buoyancy force is about 3%.

Pressure force: The pressure force is

$$\mathbf{F}_p=\tfrac{4}{3}\rho_l\pi a^3\left(\frac{D\mathbf{U}_l}{Dt}\right), \tag{8}$$

where DU_l/Dt is the local fluid (tracer particle) acceleration. The above expression is obtained by combining the viscous and pressure gradient terms in the Navier–Stokes equation to obtain the total force due to the stresses acting on the sphere (Maxey and Riley[6]). As discussed before (also see Appendix A), the error in liquid acceleration varies between 6% to 12%. Combined with the small error in bubble radius, the uncertainty in pressure force varies between 6% to 13%.

Inertia (added mass) force: A general expression for the inertia force is

$$\mathbf{F}_i=-\frac{4}{3}\pi a^3\left[\rho_b\frac{d\mathbf{U}_b}{dt}+m_a\rho_l\left(\frac{d\mathbf{U}_b}{dt}-\frac{D\mathbf{U}_l}{Dt}\right)\right], \tag{9}$$

where $d\mathbf{U}_b/dt$ is the Lagrangian bubble acceleration and m_a is the added mass coefficient. For a bubble, the first term is negligible and the inertia force is simply the added mass effect. Based on recent numerical (Chang[13]) and experimental (Naciri[4]) results, m_a is 0.5, provided the bubble is nearly spherical. The accuracy of the inertial force is fairly low, since its value is determined by subtracting accelerations. Typical relative errors in its measurement vary between 22%, when close to the vortex, to 43% when the acceleration is low. However, in most measurements, the magnitude of this force is small and consequently, the large relative error has little effect on the results.

Bassett force: Bassett forces arise as an integrated effect of the interactions of a bubble with its own wake. In the case of Stokes flow past a sphere, this force is

$$\mathbf{F}_b=6\pi a^2\mu\int_0^t\frac{d(\mathbf{U}_b-\mathbf{U}_l)/d\tau}{\sqrt{\pi\nu(t-\tau)}}d\tau. \tag{10}$$

At Reynolds numbers greater than one, the Bassett force is expected to be smaller than the result of Eq. (10). As discussed by Mei *et al.*,[14] the kernel behaves as $t^{-1/2}$ only for short times and decays at a faster rate at larger times and Reynolds numbers. Using this equation as the upper limit, we calculated the Bassett force for the entire trajectory of a 707μm diameter bubble. Details of this analysis are provided in Appendix B. As shown there, the magnitude of the Bassett force is less than 6% of the buoyancy force for most of the present experimental conditions. Consequently this force is neglected in the following force balance.

Drag and lift forces: The pressure, buoyancy, and inertia forces on a bubble must be balanced by drag and lift. The drag, $\mathbf{F}_d$ is parallel to the relative velocity between the bubble and the liquid and the lift, $\mathbf{F}_l$, is perpendicular to it. The method used to determine these forces is illustrated in Figs. 3(b)–7(b), which contain scaled vectors of forces and velocities. The pressure, buoyancy, and inertia forces are first calculated using Eqs. (7)–(9). Then, the force required to balance them, $\mathbf{F}_r$, is decomposed into two components to obtain the drag and the lift [Eq. (11)]

$$\begin{gathered}\mathbf{F}_d+\mathbf{F}_l=-(\mathbf{F}_g+\mathbf{F}_p+\mathbf{F}_i)=\mathbf{F}_r,\\ \mathbf{F}_d=\frac{\mathbf{F}_r\cdot\mathbf{U}_{\text{rel}}}{|\mathbf{U}_{\text{rel}}|},\quad \mathbf{F}_l=\mathbf{F}_r-\mathbf{F}_d.\end{gathered} \tag{11}$$

Adopting typical expressions, the results will be presented in terms of lift and drag coefficients, C_l and C_d;

$$C_d=\frac{|\mathbf{F}_d|}{0.5\rho\pi a^2U_{\text{rel}}^2}\quad\text{and}\quad C_l=\frac{|\mathbf{F}_l|}{0.5\rho\pi a^2U_{\text{rel}}^2}. \tag{12}$$

To estimate the accuracy in measuring these coefficients, one has to account for errors in the pressure, buoyancy, inertia, and Bassett forces, as well as in the direction of the relative velocity. Combining these effects, the uncertainty in the drag force varies between 3% to 6%. The uncertainty in the lift force is higher. Far from the vortex center, where the lift is very low, the relative error can be as high as 49% while closer to the core, the error is reduced to 14%. Typical relative errors are around 20%.

C. Results

Several characteristic samples of force and velocity diagrams in different sections of the vortex are presented in Figs. 3(b)–7(b). As is evident from the results, the orientations and magnitudes of the forces vary significantly, depending on the location of the bubble. When the bubble is located far from the center [Fig. 4(b)] the added mass and pressure forces are small. The buoyancy and relative velocity are almost parallel, implying that the lift force is negligible and that the buoyancy is balanced by the drag force. This result is consistent with our expectations, since the vorticity is very low in this region, and one would expect a weak lift force.

As the bubble is drawn closer to the vortex core [Figs. 5(b)–7(b)], the pressure force, vorticity, and resulting lift force increase. For the present test conditions, namely bubble diameters ranging between 500 and 800 μm, Reynolds numbers (based on the relative velocity) between 20 and 80, and vorticity between 2 and 20 s^{-1}, the lift coefficient can reach values that are as high as 35% of the drag. Specific trends with vorticity and Reynolds number are summarized in the following subsections.

1. Drag coefficient

The measured drag coefficients are plotted, along with a "standard" drag curve for a solid sphere, in Fig. 8. The empirical expression is valid for Re<800 with an accuracy of 5% (Schiller and Nauman[27]). As is evident from the results, the measured C_d for bubbles entrained by a vortex is quite close to that of solid body in quiescent fluid. The no-slip boundary condition on the bubble surface is probably a result of accumulation of impurities (Harper[2]). It is impossible to purify the water due to the presence of seed particles.

We also observe that vorticity has little effect on the measured drag coefficient. For the range of vorticity studied ($0.5<4\omega a^2/\nu<15$, where ω is the local vorticity), the variation in C_d is within our scatter range. This trend is consistent with the numerical studies of Dandy and Dwyer[22] (sphere in linear shear flow), Ingham and Tang[28] (rotating cylinder in uniform flow), and Naciri[4] (bubble within a rotating cylinder). The effect of acceleration cannot be quantified in the present experiment since the acceleration numbers are small (typical values are between −0.2 and 0.2).

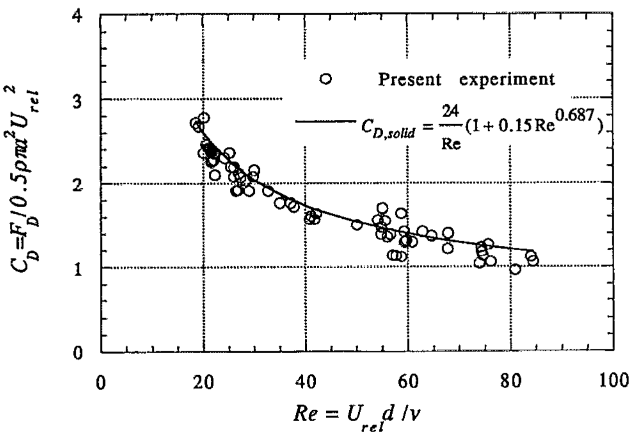

FIG. 8. Measured drag coefficient for a bubble along with an empirical drag curve for a solid sphere (Schiller and Nauman[27]).

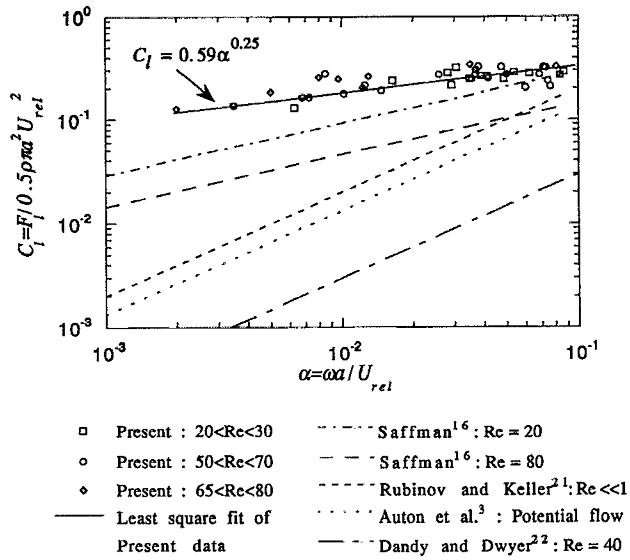

FIG. 10. A comparison of the present lift coefficients to theoretical and numerical models.

2. Lift coefficient

The measured lift coefficients are compared with available experimental results in Fig. 9 and with theoretical predictions in Fig. 10. Figure 9 includes data obtained by Naciri[4] for a stationary, but free bubble located within a rotating cylinder, as well as Barkla and Auchterlonie's,[23] Tri *et al.*'s,[24] and Tsuji *et al.*'s[10] measurements performed with spinning spheres. The latter paper does not provide specific data points and the line in Fig. 9 is estimated from their curve for C_l. Our data demonstrates that for 20<Re<80 and $0.01<\alpha<0.1$ ($\alpha=\omega a/U_{\rm rel}$), C_l of a free bubble does not vary with the Reynolds number. This conclusion is consistent with Naciri's results, as well as with Tsuji *et al.*'s and Barkla and Auchterlonie's data, which are measured at higher Reynolds numbers. Tri *et al.*'s results, however, do exhibit a considerable dependence of C_l on Re. This disagreement may be a result of their experimental procedures, in which both the spin and relative velocities are forced externally. In all the other experiments, either the trajectory or the spin velocity (or both) are unforced. Consequently, as Saffman[16] already realized, the bubble or particle then moves and spins at a rate that minimizes the net torque on its surface. However, if the sphere is spun and forced to move at a certain speed, the viscous stresses are altered to balance the external torque. Consequently, in experiments where both the spin and motion are forced, the flow structures are different.

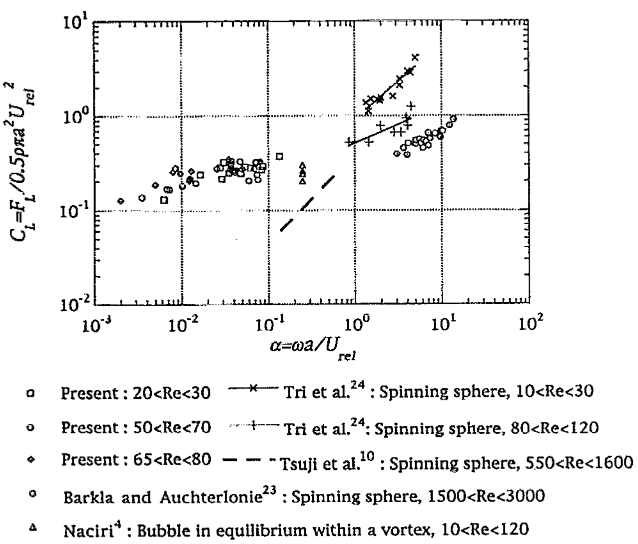

FIG. 9. A comparison of the present lift coefficients to other measurements.

The magnitude of the present lift coefficients, which range from 0.1 to 0.3, agree with Naciri's data. The experiments with spinning spheres provide widely different values for C_l, of which Barkla and Auchterlonie's results seem to be the most consistent with the present trends.

Figure 10 compares our measurements to Auton *et al.*'s[3] potential flow model, Dandy *et al.*'s[22] numerical results for a *fixed* sphere in a uniform shear flow, Saffman's[16] solution for a free sphere in a shear flow, and Rubinov's[21] model for a spinning sphere in a uniform flow. The latter two are valid only at Re≪1. For comparison purposes we substitute the present flow conditions (Re=20 and 80) in their equations, recognizing that this exercise extrapolates the solutions beyond their range of validity. It is evident from the graph that the present results do not agree with any of the theoretical models both in magnitudes as well as trends with vorticity. Depending on α, the difference can be more than an order of magnitude. The slope (power) of the present lift coefficient (Fig. 10), is approximately 0.25 (based on a least-square fit), which is less than Dandy's (slope=1.0), Auton's (slope =1.0), or Saffman's (slope=0.5) predictions. Although they are only valid for Stokes flows, Saffman's results are the closest to the present measurements. As noted before, when both the spin velocity and motion are forced externally, the entire flow structure around the bubble is altered. In Dandy's analysis the spin is zero, in Auton's, the shear stresses are zero and in Rubinov's, the motion and spin are maintained constant. Thus, none of these numerical and computational

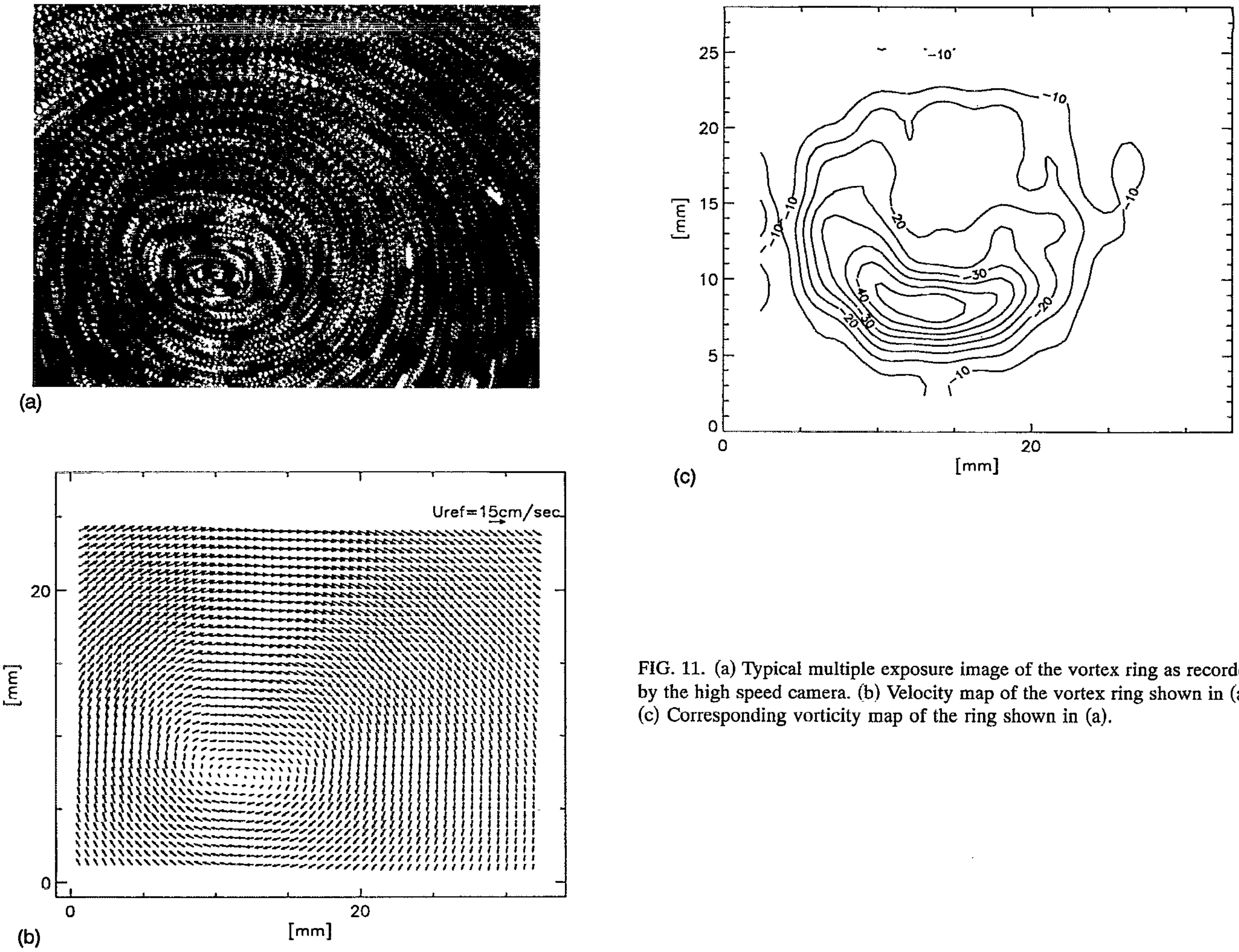

FIG. 11. (a) Typical multiple exposure image of the vortex ring as recorded by the high speed camera. (b) Velocity map of the vortex ring shown in (a). (c) Corresponding vorticity map of the ring shown in (a).

models describe conditions which are consistent with free bubbles and the discrepancy between results should be expected.

Although one can reason and explain why the present trends do not agree with existing theories, we still do not have an explanation for the present results. It seems that one has to solve for the flow structure around the bubble (presumably numerically), satisfying torque conditions on its surface, in order to understand the causes and effects involved. Unknown at this stage, is the relationship between the external vorticity and bubble spin and their combined impact on the lift. Some clue on the former is provided by the experiments of Poe and Acrivos,[29] who measured the spin velocities of a sphere in a pure shear flow (no mean flow) and found them to range between 0.45 and 0.5 of the externally imposed shear. However, at the present time, to the best of our knowledge, nobody has computed the flow around a *free* sphere in a nonuniform flow.

III. PREDICTIONS OF BUBBLE TRAJECTORY

In this section, we use the measured drag and lift coefficients to compute the trajectory of a bubble and compare the result with experimental observations. As an example, we focus on the entrainment of a 707 μm bubble. Assuming an added mass coefficient of 0.5, the equation governing its motion is

$$\frac{d\mathbf{U}_b}{dt} = -2\mathbf{g} + 3\left(\frac{\partial \mathbf{U}_l}{\partial t} + (\mathbf{U}_l \cdot \nabla)\mathbf{U}_l\right) + \frac{3}{4a} C_d |\mathbf{U}_{\mathrm{rel}}| \mathbf{U}_{\mathrm{rel}} + \frac{3}{4a} C_l |\mathbf{U}_{\mathrm{rel}}|^2 \frac{\mathbf{U}_{\mathrm{rel}} \times \boldsymbol{\omega}}{|\mathbf{U}_{\mathrm{rel}}||\boldsymbol{\omega}|}. \tag{13}$$

The terms on the right-hand side of this equation are due to to buoyancy, liquid stresses, drag, and lift, respectively (the Bassett force is neglected, as discussed in Appendix B). Here, C_d and C_l, can be determined from a least-square fit of the data provided in Figs. 8 and 10, respectively. Thus, to compute the acceleration and consequently the motion of the bubble, one only needs to know the velocity field of the liquid (from which the acceleration and vorticity can be calculated) and the initial conditions of the bubble. This information is obtained using PIV and the experimental setup described in Sec. II. However, in order to compare the results to the actual bubble trajectory we use *two* cameras. The first, a 35 mm movie camera, records multiple frames of the particles at 20 frames per second [a typical image is provided in Fig. 11(a)] while a second 70 mm still camera, records an extended single frame of the entire trajectory of the entrained bubble (Fig. 12). The images of the movie camera are used to map the velocity field of the vortex at discrete time intervals. An autocorrelation technique is employed with an interrogation window size of 1.2×1.2 mm. Data is obtained every 0.6 mm, by stepping at half window size intervals.

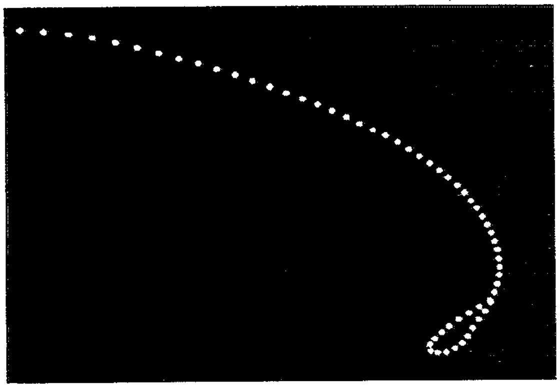

FIG. 12. Trajectory of a 707 μm bubble as it is entrained into the core of a laminar vortex.

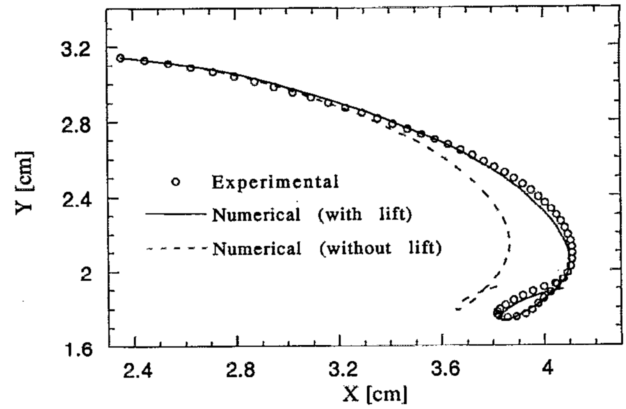

FIG. 13. Comparison of bubble trajectories obtained experimentally and by numerical integration of Eq. (13).

Each window contains at least three particle pairs and the estimated error in measurement of the mean velocity is less than 1.5% (Chu *et al.*[30]). The velocity and vorticity fields obtained by analyzing the image in Fig. 11(a) are plotted in Figs. 11(b) and 11(c), respectively.

Using a second-order finite difference scheme, with a step size of 0.6 mm, the spatial gradients and vorticity field within the vortex are calculated. The unsteady term in Eq. (13), $(\partial \mathbf{U}_l/\partial t)$, is due to the convection of the vortex and the unsteady variations within the ring structure. Its magnitude is determined by comparing the velocity maps obtained from three successive frames of the movie camera, and computing the change in velocity at the same physical locations. Under the present flow conditions (laminar vortex), examination of the data clearly shows that convection of the vortex is the primary contributor to the unsteady term. The overall uncertainty in the measurement of the right-hand side of equation, including the absence of the Bassett force in the equation is 11%.

The trajectory of the bubble is now predicted by numerically integrating Eq. (13). A fourth-order Runge–Kutta scheme with a time step of 0.01 ms is used. The initial location and velocity of the bubble are chosen to match the experimental conditions. Using the fluid velocity and vorticity at that location, C_d and C_l are determined. The entire right-hand side is now known and can be integrated to obtain the new bubble velocity and location. The results are plotted and compared with the experimental trajectory in Fig. 13. The agreement between the numerical and experimental results is clearly evident and discrepancies are well within the error limits of the present experiments. Also plotted in Fig. 13 is a hypothetical trajectory of the same bubble when the lift force is neglected. In this particular case, the lift force increases the overall entrainment time by 7.5%. However, focusing on regions with significant vorticity, starting from $x=3.2$ cm in Fig. 13, the lift increases the entrainment time by 20%. It clearly has a significant impact on the trajectory of the bubble.

IV. CONCLUSIONS

Instantaneous velocity and acceleration measurements of bubbles and the fluid surrounding them are utilized for determining their lift and drag coefficients during entrainment by a vortex. The drag coefficient, and its dependence on Reynolds number agree with existing steady-state data. Vorticity does not seem to have a significant effect on the C_d, which is consistent with numerical studies of Dandy and Dwyer[22] and Ingham and Tang.[28] Within the present test conditions, the lift coefficient is approximately proportional to the fourth root of the dimensionless vorticity. This trend differs from existing theoretical and numerical models. Differences in boundary conditions and/or Reynolds numbers are probable causes for the discrepancy. Varying in magnitude between 0.1 and 0.3, the present results agree with Naciri's[4] data, which is the only other available measurement of lift forces on bubbles. Both results show little dependence on the Reynolds number. We cannot compare the dependence on vorticity since all of Naciri's measurements are performed at the same dimensionless vorticity. For further verification, the measured drag and lift coefficients are used for computing the trajectory of a 707 μm bubble. The results compare well with experimental observations.

ACKNOWLEDGMENTS

This project was sponsored by the Office of Naval Research under Grant No. N00014-91-J-1176. The authors would like to knowledge the technical assistance of Mr. Van Hooijdonk and Mr. John Woomer.

APPENDIX A: ERRORS IN VELOCITY, ACCELERATION, AND VORTICITY MEASUREMENTS

The uncertainty in our results is affected by errors in measuring the particle and bubble displacements, as well as by the interpolation scheme. Methods to determine and quantify the effect of these errors on our results are discussed in this appendix. Also included is an assessment of our ability to determine the local fluid velocity and the acceleration from traces of four particles.

Measurement error: As noted before, the uncertainty in measuring the displacement is 0.4 pixels. The corresponding error in the fluid velocity, which is determined by interpolation, ranges from 0.23 to 0.29 pixels. Thus, by selecting a magnification of 1300 pixels per cm, with typical particle displacements between 80 and 120 pixels, it is possible to maintain a relative error of 0.25% to 0.35%. The bubble velocity still has a measurement error of 0.4 pixels and its relative error varies between 0.5% and 0.9%.

Since the acceleration is obtained from the difference between two measured velocities, the uncertainty in its measurement is 0.57 pixels [$\sqrt{2\times(0.4)^2}$], which is equivalent to 37.9 cm/s^2. After interpolation, the absolute error in the liquid acceleration is 22–27 cm/s^2, and the corresponding relative error is between 6% to 12%. The relative error in the bubble acceleration varies considerably depending on the magnitude of its acceleration. Far from the vortex center, it can be as high as 50%, while around the vortex core, where the acceleration is larger, the uncertainty decreases to typical values of 15% with a minimum of 9%. Typical values for the relative error in the vorticity vary between 1.1% close to the vortex core, to 10% in the outer perimeter of the vortex.

Temporal averaging error: This error occurs as a result of assuming a straight line trajectory between traces of an individual particle. To quantify this error, the velocity field is modeled as a thin tube vortex ring, which is described by Batchelor.[31] Selecting a particular site, the location of a particle at three instants is computed using the theoretical flow field. The corresponding particle velocity is estimated from its discrete locations and compared to the actual mean value. As expected, the error in estimating the velocity from the particle displacement increases with the delay between pulses and with decreasing distance from the vortex center. However, for all the data presented in this paper, the temporal averaging error in velocity is less than 0.1%, while the error in acceleration is less than 0.2%.

Interpolation error: Using the same vortex model, the accuracy of obtaining velocity and acceleration information from neighboring particle traces is also estimated. The velocity and accelerations at four points, located around the site of interest is first determined. The present interpolation scheme is then used to estimate the velocity and acceleration at the desired site and compared to the exact values. Typical errors range between 0.3% to 2.5% for the velocity and 2% and 5% for the acceleration.

We can now determine the overall uncertainties in the velocity and acceleration due to measurement, temporal averaging and spatial interpolation errors. Typical uncertainties for the bubble and interpolated fluid velocities are 0.6%–0.9% and 0.4%–2.3%, respectively. Uncertainties in acceleration vary considerably, between 9% to 48% for the bubble (high levels of uncertainty occur only in regions with low acceleration), and between 6% to 12% for the fluid.

APPENDIX B: ESTIMATE OF THE BASSETT FORCE

In this appendix, we estimate the magnitude of the Bassett force on the same bubble discussed in Sec. III. Equation (10) is used and as mentioned earlier, this expression can serve as an upper bound for the Bassett force at Reynolds numbers exceeding 1. The unknown in this equation is the relative acceleration of the bubble, which is determined from the recorded PIV data [Fig. 11(a)] and the bubble trajectory (Fig. 12).

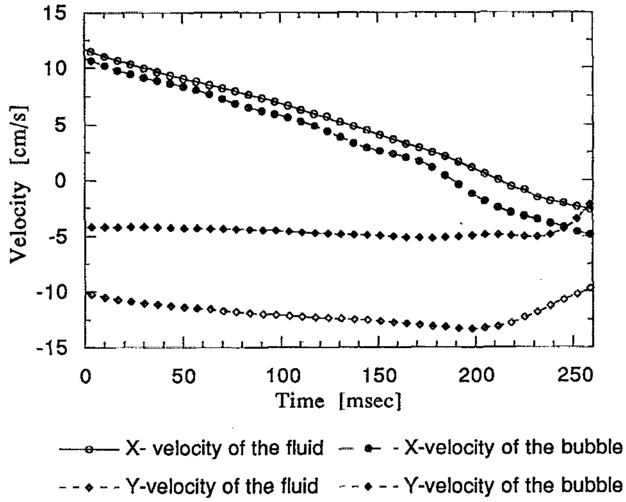

FIG. 14. Time history of bubble and particle velocities during entrainment of the bubble.

Procedures for determining the fluid velocity, using autocorrelation, are described in Sec. III of this paper. In addition, the bubble traces shown in Fig. 12 are analyzed to obtain the trajectory and velocity history of the bubble during entrainment. The image is magnified so that each trace is at least 20 pixels wide with a mean displacement greater than 40 pixels. At this magnification, the estimated accuracy in the measurement of the velocity of the bubble is 1%. Each trace of the bubble is matched in time and space to its location on the images of the movie camera. The history of the relative velocity of the bubble is then determined along the bubble path (Fig. 14). The relative velocity is differentiated in time to obtain the relative acceleration of the bubble (Fig. 15). The error in the measurement of the relative acceleration is high, about 35%, but since our only intention is to obtain an order of magnitude estimate, we can still use this data.

The measured acceleration is substituted into Eq. (10) and the Bassett force is computed using a Newton–Cotes numerical integration scheme. The computed force is decomposed into X, Y components in a Cartesian frame, as well as

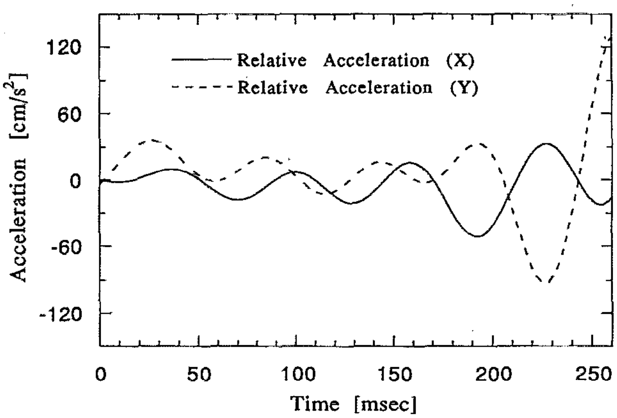

FIG. 15. Plot of the relative acceleration of the bubble during entrainment.

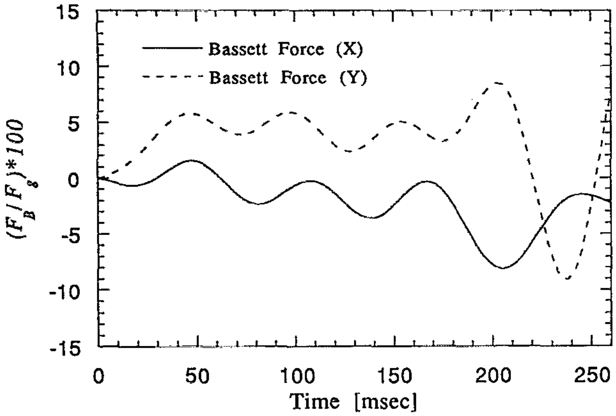

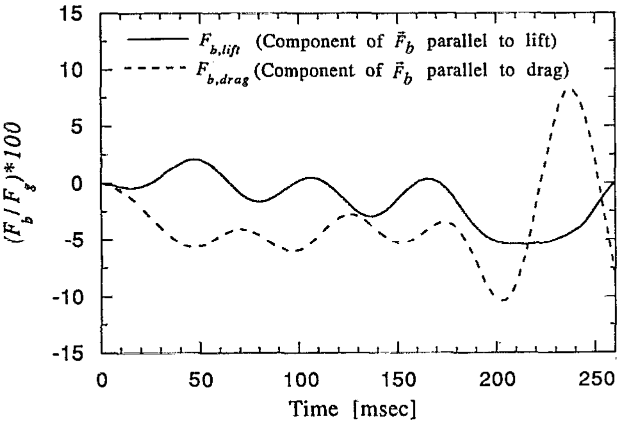

FIG. 16. (a) Estimate of the Bassett force acting on a 707 μm bubble during entrainment, resolved into X, Y components in a Cartesian frame. (b) Resolved into components parallel to the drag and lift forces.

into components parallel to the drag and lift forces [Figs. 16(a) and 16(b)]. As is evident from the results, the estimated Bassett force in the direction of the drag, $|\mathbf{F}_{b,\text{drag}}|$, is less than 5% of the buoyancy force for most of the trajectory. The largest $|\mathbf{F}_{b,\text{drag}}|$, is 10% of $|\mathbf{F}_g|$ and the corresponding drag force at the same time is about 160% of $|\mathbf{F}_g|$. Thus for the present experiment, the maximum relative error in the measurement of the drag introduced by neglecting the Bassett force, is less than 6%. The estimated Bassett force in the direction of lift, $|\mathbf{F}_{b,\text{lift}}|$, is less than 2.5% of $|\mathbf{F}_g|$ for most of the entrainment process and increases to 5% of $|\mathbf{F}_g|$ only during the final 60 ms. The corresponding lift force, computed using the data in Figs. 9 and 10, varies between 15%–25% of $|\mathbf{F}_g|$ during most of the entrainment process and increases to 35% during the final stage. Thus, the estimated $|\mathbf{F}_{b,\text{lift}}|$ is at most 16% of the lift force for the entire entrainment process. Keeping our error levels in mind, our assumption of negligible Bassett force is valid.

[1]R. Clift, J. R. Grace, and M. E. Weber, *Bubbles, Drops, and Particles* (Academic, New York, 1978).

[2]J. F. Harper, "The motion of bubbles and drops through liquids," Adv. Appl. Mech. **12**, 59 (1972).

[3]T. R. Auton, J. C. R. Hunt, and M. Prud'homme, "The force excerted on a body in inviscid unsteady non-uniform rotational flow," J. Fluid Mech. **197**, 241 (1988).

[4]M. A. Naciri,"Contribution à l'étude des forces exercées par un liquide sur une bulle de gaz: portance, masse ajoutée et interactions hydrodynamiques," Ph.D. thesis, L'ecole Centrale De Lyon, Lyons, 1992.

[5]A. B. Bassett, *A Treatise on Hydrodynamics* (Dover, New York, 1961).

[6]M. R. Maxey and J. J. Riley, "Equation of motion for a small rigid sphere in a nonuniform flow," Phys. Fluids **26**, 883 (1983).

[7]S. Temkin and H. K. Mehta, "Droplet drag in an accelerating and decelerating flow," J. Fluid Mech. **116**, 297 (1982).

[8]R. Li and M. Boulos, "Modeling of unsteady flow around accelerating sphere at moderate Reynolds numbers," Can. J. Chem. Eng. **71**, 837 (1993).

[9]F. Odar and W. S. Hamilton, "Forces on a sphere accelerating in a viscous fluid," J. Fluid Mech. **18**, 302 (1964).

[10]Y. Tsuji, Y. Morikawa, and O. Mizuno, "Experimental measurement of the Magnus force on a rotating sphere at low Reynolds numbers," J. Fluids Eng. **107**, 484 (1985).

[11]F. Odar, "Verification of the proposed equation for calculation of the forces on a sphere accelerating in a viscous fluid," J. Fluid Mech. **25**, 591 (1966).

[12]F. Odar, "Unsteady motion of a sphere along a circular path in a viscous fluid," J. Appl. Mech. **90**, 652 (1968).

[13]E. J. M. Chang, "Accelerated motion of rigid spheres in unsteady flows at low to moderate Reynolds numbers," Ph.D. thesis, Brown University, 1992.

[14]R. Mei, C. J. Lawrence, and R. J. Adrian, "Unsteady drag on a sphere at finite Reynolds number with small fluctuations in the free-stream velocity," J. Fluid Mech. **233**, 613 (1991).

[15]R. Mei and R. J. Adrian, "Flow past a sphere with an oscillation in the free-stream velocity and unsteady drag at finite Reynolds number," J. Fluid Mech. **237**, 323 (1992).

[16]P. G. Saffman, "The lift on a small sphere in a slow shear flow," J. Fluid Mech. **22**, 385 (1965); Corrigendum, J. Fluid Mech. **31**, 624 (1968).

[17]J. B. Mclaughlin,"Inertial migration of a small sphere in a linear shear flow," J. Fluid Mech. **224**, 261 (1991).

[18]E. Y. Harper and I. D. Chang, "Maximum dissipation resulting from lift in a slow viscous shear flow," J. Fluid Mech. **33**, 209 (1968).

[19]D. A. Drew, "The force on a small sphere in a slow viscous flow," J. Fluid Mech. **88**, 393 (1978).

[20]R. G. Cox and H. Brenner, "The lateral migration of solid particles in Poisuille flow: I Theory," Chem. Eng. Sci. **23**, 147 (1968).

[21]S. I. Rubinov and J. B. Keller, "The transverse force on a spinning sphere moving in a viscous fluid," J. Fluid Mech. **11**, 447 (1961).

[22]D. S. Dandy and H. A. Dwyer, "A sphere in a shear flow at finite Reynolds number: Effect of shear on particle lift, drag and heat transfer," J. Fluid Mech. **216**, 381 (1990).

[23]H. M. Barkla and L. J. Auchterlonie, "The Magnus or Robins effect on rotating spheres," J. Fluid Mech. **47**, 437 (1971).

[24]B. D. Tri, B. Oesterlé, and F. Deneu, "Premiers résulats sur la portance d'une sphère en rotation aux nombres de Reynolds intermédiaies," C. R. Acad. Sci. Paris Ser. II **311**, 27 (1990).

[25]B. Ran and J. Katz, "The response of microscopic bubbles to sudden changes in the ambient pressure," J. Fluid Mech. **224**, 91 (1991).

[26]G. Sridhar, B. Ran, and J. Katz, "Implementation of particle image velocimetry to multi-phase flows," Cavitation Multiphase Flow Forum **109**, 205 (1991).

[27]L. Schiller and A. Z. Nauman, "Uber de grundlegenden berechnungen bie schwerkraftaufberietung," Z. Ver. Dtsch. Ing. **77**, 318 (1933).

[28]D. B. Ingham and T. Tang, "A numerical investigation into the steady flow past a rotating cylinder at low and intermediate Reynolds numbers," J. Comput. Phys. **87**, 91 (1990).

[29]C. G. Poe and A. Acrivos, "Closed-streamline flows past rotating single cylinders and spheres: inertia effects," J. Fluid Mech. **72**, 605 (1975).

[30]S. Chu, R. Dong, and J. Katz, "Quantitative visualization of the flow within the volute of a centrifugal pump. Part A: Technique," J. Fluids Eng. **114**, 390 (1992).

[31]G. K. Batchelor, *An Introduction to Fluid Dynamics* (Cambridge University Press, Cambridge, 1967).